Project 2526 | September 2026

SJSU SAN JOSÉ STATE UNIVERSITY

MTI MINETA TRANSPORTATION INSTITUTE

Reducing Drag of Vehicles with Half-Stepped Cylinder Surfaces - Part I: Numerical Optimization

Ryan Moffit   Hamid Rahai, PhD   Komal Gada, PhD

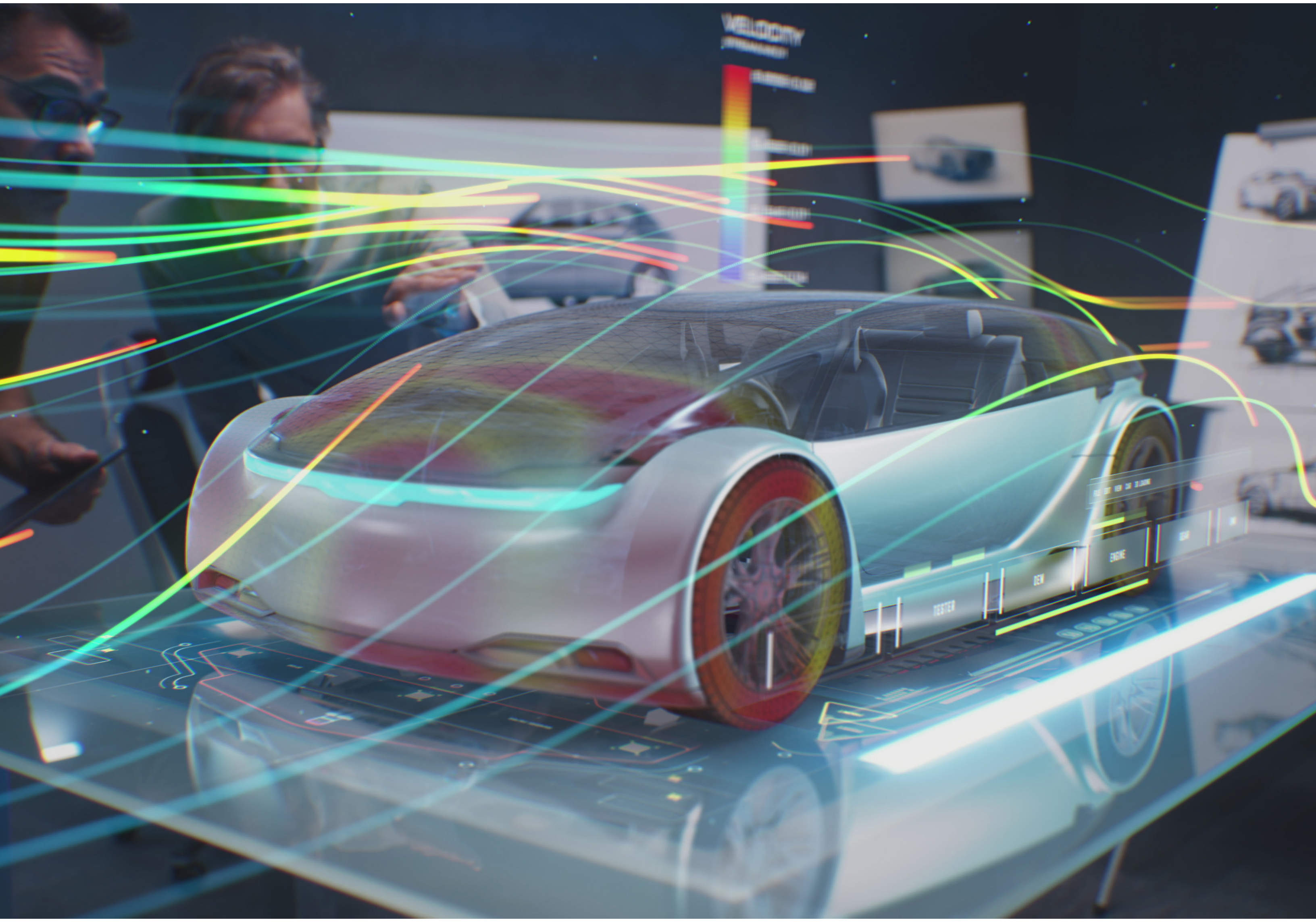

CSUTC California State University Transportation Consortium

CALIFORNIA STATE UNIVERSITY LONG BEACH

MINETA TRANSPORTATION INSTITUTE

Founded in 1991, the Mineta Transportation Institute (MTI), an organized research and training unit in partnership with the Lucas College and Graduate School of Business at San José State University (SJSU), increases mobility for all by improving the safety, efficiency, accessibility, and convenience of our nation's transportation system. Through research, education, workforce development, and technology transfer, we help create a connected world. MTI leads the California State University Transportation Consortium (CSUTC) funded by the State of California through Senate Bill 1 and the Rail Resilience to Severe Weather: Training and Research Program (RR2SW) funded by the Federal Railroad Administration. MTI focuses on three primary responsibilities:

Research

MTI conducts multi-disciplinary research focused on surface transportation that contributes to effective decision making. Research areas include: active transportation; planning and policy; security and counterterrorism; sustainable transportation and land use; transit and passenger rail; transportation engineering; transportation finance; transportation technology; and workforce and labor. MTI research publications undergo expert peer review to ensure the quality of the research.

Education and Workforce Development

To ensure the efficient movement of people and goods, we must prepare the next generation of skilled transportation professionals who can lead a thriving, forward-thinking transportation industry for a more connected world. To help achieve this, MTI sponsors a suite of workforce development and education opportunities. The Institute supports educational programs offered by the Lucas Graduate School of Business: a Master of Science in Transportation Management, plus graduate certificates that include High-Speed and Intercity Rail Management and Transportation Security Management. These flexible programs offer live online classes so that working transportation professionals can pursue an advanced degree regardless of their location.

Information and Technology Transfer

MTI utilizes a diverse array of dissemination methods and media to ensure research results reach those responsible for managing change. These methods include publication, seminars, workshops, websites, social media, webinars, and other technology transfer mechanisms. Additionally, MTI promotes the availability of completed research to professional organizations and works to integrate the research findings into the graduate education program. MTI's extensive collection of transportation-related publications is integrated into San José State University's world-class Martin Luther King, Jr. Library.

Report 26-31

Reducing Drag of Vehicles with Half-Stepped Cylinder Surfaces
Part I: Numerical Optimization

Ryan Moffit
Hamid Rahai, PhD
Komal Gada, PhD

September 2026

A publication of the
Mineta Transportation Institute
Created by Congress in 1991

College of Business
San José State University
San José, CA 95192-0219

Technical Report Documentation Page

1. Report No.	2. Government Accession No.	3. Recipient's Catalog No.
26-31		

4. Title and Subtitle	5. Report Date
Reducing Drag of Vehicles with Half-Stepped Cylinder Surfaces Part I: Numerical Optimization	September 2026
	6. Performing Organization Code
7. Authors Ryan Moffit Hamid Rahai, PhD Komal Gada, PhD	**8. Performing Organization Report** CA-MTI-2525
9. Performing Organization Name and Address Mineta Transportation Institute College of Business San José State University San José, CA 95192-0219	**10. Work Unit No.** **11. Contract or Grant No.** SB1-SJAUX_2023-26
12. Sponsoring Agency Name and Address State of California SB1 2017/2018 Trustees of the California State University Sponsored Programs Administration 401 Golden Shore, 5th Floor Long Beach, CA 90802	**13. Type of Report and Period Covered** **14. Sponsoring Agency Code**

15. Supplemental Notes

10.31979/mti.2026.2525

16. Abstract

Aerodynamic drag is a major source of energy loss for vehicles, increasing fuel consumption, reducing the driving range of electric vehicles, and contributing to greenhouse gas emissions. For a vehicle, the major components of its drag are pressure and viscous drag. Engineers have developed a variety of strategies to reduce drag, including streamlined vehicle designs, surface modifications, and devices that alter airflow around the vehicle. This research focuses on reducing the viscous drag. Specifically, this study investigates whether microscopic surface features called half-stepped cylinder arrays can reduce skin friction by altering the turbulent boundary layer and promoting smoother airflow near the vehicle surface Using computational fluid dynamics simulations and numerical optimization, the researchers evaluated different cylinder sizes and spacing to identify a surface design that minimized skin friction on a simulated flat plate. The results indicate that when the cylinder's dimensions are less than 1% of the boundary layer thickness, there is over 33% reduction in average skin friction. The findings demonstrate that carefully designed microscopic surface structures can substantially reduce skin friction in turbulent flows, which can contribute to improved aerodynamic efficiency and lower vehicle energy consumption. Although additional research is needed to validate these results on full-scale vehicles and under real-world operating conditions, this approach shows promise as a passive aerodynamic technology that could improve vehicle efficiency, extend electric vehicle range, and reduce transportation-related energy use and emissions.

17. Key Words	18. Distribution Statement		
Air resistance, climate change, aerodynamics, drag	No restrictions. This document is available to the public through The National Technical Information Service, Springfield, VA 22161.		
19. Security Classif. (of this report) Unclassified	**20. Security Classif. (of this page)** Unclassified	**21. No. of Pages** 36	**22. Price**

Form DOT F 1700.7 (8-72)

DOI: 10.31979/mti.2026.2525

Mineta Transportation Institute
College of Business
San José State University
San José, CA 95192-0219

Email: mineta-institute@sjsu.edu

transweb.sjsu.edu/research/2525

Acknowledgments

Funding for this research was provided by the California State University Transportation Consortium through the State of California's Senate Bill 1, the Road Repair and Accountability Act of 2017. The authors thank Lisa Rose and Editing Press for editorial services, as well as MTI staff Project Assistant, Cameron Simons, and Graphic Design Assistant, Katerina Earnest.

The authors would like to thank Mr. Waled Raban, Account Manager, Ansys Southwest, USA, for his continuous support in providing an Ansys HPC license for the present research.

A provisional patent on optimized half-stepped cylinder geometries for surface drag reduction has been filed with the US Patent and Trademark Office. A full patent application is pending.

Contents

List of Figures

List of Tables

Executive Summary

Transportation is a major source of greenhouse gas emissions in California and the nation, with direct tailpipe emissions accounting for over 40% of the state's greenhouse gas emissions. California has set goals to reduce greenhouse gas emissions 40% below 1990 levels by 2030 and add five million zero-emission vehicles to California's roads by 2030. The executive orders N-19-19 and N-79-20[1,2] require the Department of General Services to maximize the reduction of greenhouse gas emissions from the state fleet and promote zero-emission vehicle purchasing in state and local government fleets.

Aligned with the California climate action goals, the transportation sector and package delivery services are transitioning their fleets to low-emission and electric vehicles. Amazon has set a goal of 100,000 electric delivery vans by 2030, and FedEx aims to achieve 100% electric delivery by 2040.

For a vehicle, the major components of its drag are pressure and viscous drag. Reducing its drag (cars, planes, trains, ships) reduces emissions and increases travel range for both gas- and electric-powered vehicles. Methods for reducing drag include improved aerodynamics, surface modifications, and add-ons that change the pressure differential across the vehicles. Here, we have focused on reducing the viscous drag. We used numerical optimization and computational fluid dynamics to develop an optimized half-stepped cylinder surface to reduce the drag of a flat plate turbulent boundary layer. The results indicate that when the cylinder's dimensions are less than 1% of the boundary layer thickness, there is over a 33% reduction in average skin friction.

1. Introduction

A boundary layer is a layer near the surface where viscous effects are significant. At low speeds, where the boundary layer is considered to be laminar, the viscous effects are the only surface force resisting the motion of the fluid and contributing to the viscous drag. However, at high speeds when the boundary layer is turbulent, the total stress is the summation of laminar and turbulent shear stress, where the turbulent shear stress is much higher than the laminar shear stress due to its higher momentum transfer and steeper velocity gradient. Skin friction represents the resistance to flow due to the total stress. Reducing turbulent shear stress or relaminarizing the turbulent boundary layer reduces the total stress, skin friction, and overall drag of a flat-plate boundary layer at high Reynolds numbers.

Passive techniques that interfere with boundary layer structure, such as grooves, vortex generators, and large eddy break-up (LEBUs) devices, have been deployed for controlling boundary layer separation, reducing drag, and increasing the maximum lift of airfoils[3,4]. Adding transverse rectangular grooves to the main flow on the surface has been shown to improve the pressure recovery of wide-angle diffusers and delay boundary layer separation when an adverse pressure gradient was present[5-7], and streamwise grooves placed upstream of a wing-body junction have resulted in reducing the strength of the secondary flow, which contributes to the overall drag reduction in airplanes and turbomachinery[8].

A numerical investigation of airflow at a transonic speed (Mach 0.85) over the wing of the NASA high-lift Common Research Model (CRM) with and without a conformal vortex generator (CVG**)** has shown a nearly 6% improvement in lift-to-drag ratio and reduced tip vortices with CVG in place[9]. For the CRM with CVG, the tape had a width and thickness of 0.83 m and 2 mm, respectively, and covered the entire span of the wing. The tape had sawtooth-shaped cutouts, and the leading and trailing edges faced opposite each other. The base radius of the tooth was 0.5 mm with a total angle of about 30 degrees. The tape was attached to the suction side of the airfoil at 60% of the chord from its leading edge. The details of the flow characteristics showed that with the CVG in place, the non-uniformities in upstream shear stress and pressure distribution were reduced, and the skin friction downstream of the CVG was decreased by 8%.

In a turbulent boundary layer, the oscillation and lift-off of the low-speed streaks (hairpin vortices) in the near-wall region are responsible for a large fraction of its total shear stress. Placing riblets of specific dimensions constrains the growth of these streaks and reduces turbulent shear stress. To prevent these streaks from interconnecting, the spanwise separation and near-wall burst need to be increased. The spacing between two adjacent streaks is estimated as 100 wall units, with their diameters on the order of 30-40 wall units. To control these streaks, the riblet spacing should be higher than 100 wall units.

Results of several studies[10-14] on flow characteristics and the development of an optimized geometry of the riblets have shown that in a high Reynolds number laminar boundary layer over a ribbed surface, the flow inside the grooves is increasingly retarded, creating a layer of slow-moving fluid that results in lower shear stress inside the grooves, especially at the base of the grooves. This shear stress is lower than the corresponding shear stress for a smooth flat plate boundary layer. Increasing the riblet aspect ratio increases the thickness of the viscous boundary layer, and the axial vorticity within the groove decreases with increasing the length of the groove. The optimum aspect ratio for maximum shear stress reduction at zero pressure gradient was found to be near 1.

Small cavities on the surface have been shown to create a condition where the no-slip boundary condition relaxes, resulting in reduced viscous drag. The mechanism of flow through a cavity has been investigated significantly in the past[15-19]. Figure 1 shows an open cavity with separated shear layers. Self-sustained oscillation starts with a small disturbance in the shear layer. The flapping shear layer impinges on the cavity back wall, directing flow through the cavity and creating a clockwise vortex. A counterclockwise vortex is also created when cavity flow encounters the clockwise vortex. The counter-rotating vortices impinging on the shear layer amplify the disturbance, and the cycle repeats itself; at sufficiently large Reynolds numbers, for a specific cavity geometry, self-sustained oscillations are obtained with enhanced mixing. The impingement of the counter-rotating vortices on the shear layer above the cavity is the mechanism for reduced viscous drag.

Figure 1. An Open Cavity

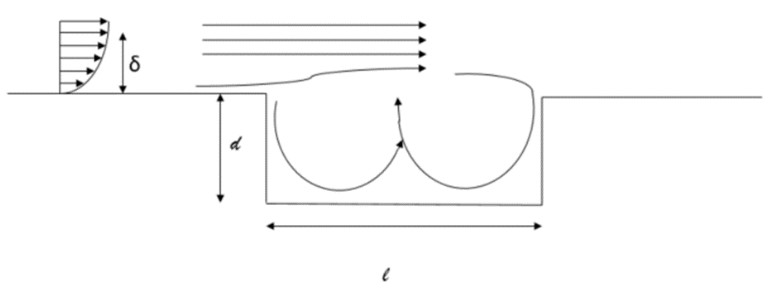

There have been extensive investigations over the past decades with conflicting results on flow characteristics around structures replicating sharkskin and denticles for drag reduction applications[20,21]. The denticle has a central primary keel or ridge similar to riblets, with some having secondary and tertiary keels. Recent results have shown increased overall drag due to increases in both form and skin friction drag. Flow around the denticle was highly three-dimensional, which contributed to increased turbulent statistics and the total drag. Superhydrophobic surfaces have been investigated for reducing the viscous shear stress of naval vessels. Studies of superhydrophobicity are rooted in water-repellent surfaces (e.g., lotus surface) where water droplets roll rather than slide over the surface. These surfaces have roughness at nano- or micro-scale sizes that reduces their wettability, resulting in increased contact angles (> 150 degrees) and reduced contact angle hysteresis, allowing the rolling of the droplets. The surface includes a series of microcavities where air is trapped between the ridges and the water layer above it, creating an air-water interface that prevents water from entering these ridges. The rolling of the droplets relaxes the no-slip boundary condition and reduces turbulent shear stress and the overall drag of the vehicle.

Recent investigations[22-30] provide details of superhydrophobic characteristics and applications, which show that for these surfaces to impact the turbulent flow, the micro-ridge spacing (w) should approach the thickness of the viscous sublayer ($w \sim y_{vsl}$). Reducing the thickness of the viscous sublayer increases the impact of the superhydrophobic surface, and increasing the Reynolds number results in a higher reduction in drag of these surfaces. At very large Reynolds numbers, an asymptotic drag reduction value could be achieved with micro ridges being higher than the viscous sublayer.

For laminar flows, increasing d (spacing between adjacent ridges) or decreasing h (the depth of the cavity) results in drag reduction and increased slip length (the distance that the drop rolls).

We have conducted a preliminary experimental investigation of a single row of half-stepped cylinders followed by a sheet of half-stepped cylinders placed on a flat plate inside a turbulent boundary layer at zero pressure gradient[31]. The ratio of the cylinder's radius to the local boundary layer thickness (r/δ_0) was 4%, and the Reynolds number based on flat plate length was 5.8 × 10^5. An estimate of the skin friction coefficient was made using the Clauser chart, and turbulence measurements were made using a single hot wire anemometer. Results showed that, with the stepped cylinder in place, the local skin friction coefficient decreases downstream of the half-stepped cylinder, with maximum drops exceeding 12% and 35%, respectively, for the single row and cylinder sheet at x/D = 13, and then gradually recovers to the corresponding value for an unperturbed flat plate at x/D = 26. Here, the reference axial distance is the aft edge of the cylinder or the last row of cylinders (for the half-stepped cylinder sheet). At x/D = 13 and further downstream, the spanwise variations of the boundary layer parameters behind the stepped cylinder were insignificant. Above the stepped cylinder, the turbulence intensity was reduced; however, in the near wake downstream, there was an increase in axial turbulence intensity attributed to the wake of the stepped cylinder.

The objective of the present investigations was to use an optimization method along with CFD to develop an optimized cylinder surface where 1) the ridges between the half-stepped cylinder rows could control the hairpin vortices to maintain the flow laminar, and 2) the spacing between the cylinders' bumps creates a micro cavity for relaxing the no-slip boundary condition for a significant reduction in surface shear stress, and thus the skin friction drag.

2. Numerical Method

A smooth flat plate 5.5 m long with variable width was used for all simulations. A trip wire of 1 mm diameter was placed 10 mm from the leading edge on the surface to trip the boundary layer and transition it to a turbulent boundary layer. The width of the flat plate was equal to the summation of the width and spacing of one row of three step cylinder segments. The half-stepped cylinders were placed 5.3 m from the flat plate leading edge in the mid-section, with the cylinders' edge facing the incoming flow. The freestream mean velocity was 10 m/s, which corresponds to an approximate Reynolds number of 2.85 x 10^6 at the streamwise distance x = 5 m, ensuring a fully developed turbulent boundary layer upstream of the cylinders.

2.1 The Half-Stepped Cylinders

Figure 2 shows the half-stepped cylinders. The spacing s, width w, and radius r (=D/2) were optimized for maximum skin friction reduction. Parametric optimizations were performed to find the optimum size of these parameters to control the boundary layer hairpin vortices and create micro-cavities for re-laminarization and to reduce the no-slip boundary condition for a significant reduction in the surface skin friction.

Figure 2. The Half-Stepped Cylinders

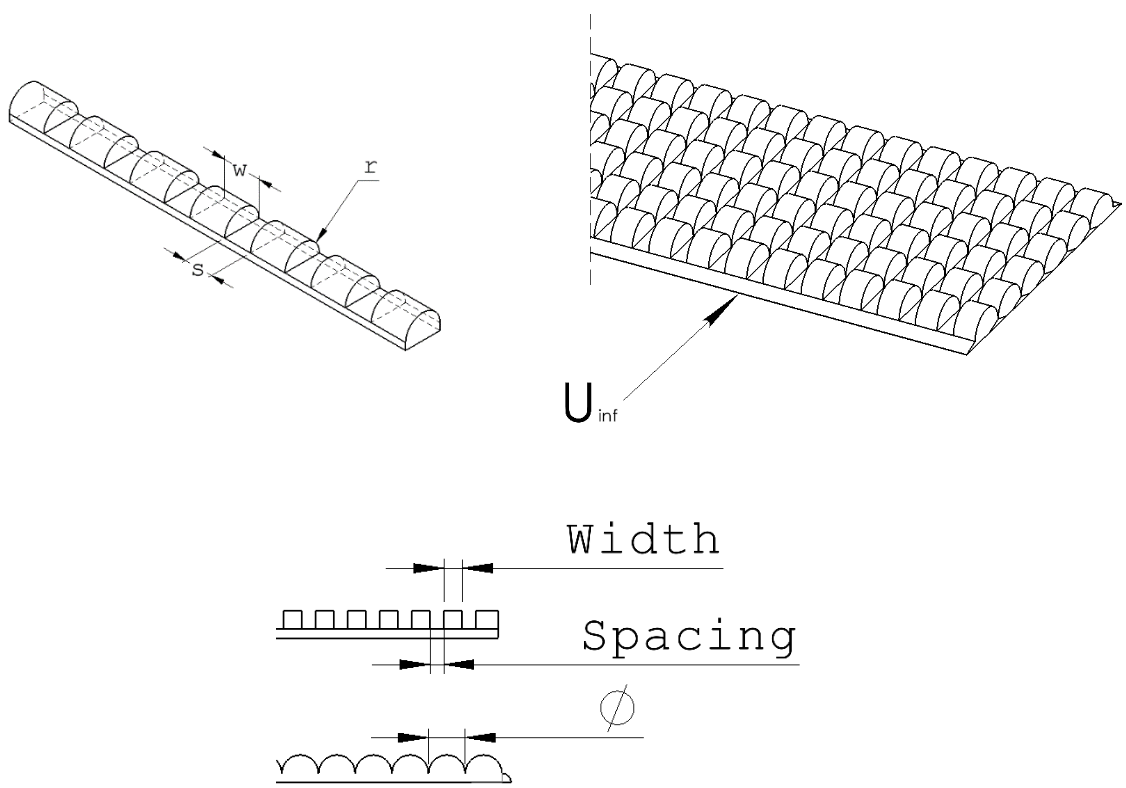

2.2 The Numerical Simulations and Optimization Process

Figure 3 shows the parametric optimization process. The optimization process started with initial conceptual geometry, followed by numerical simulations and refinement of geometrical dimensions to identify the optimum geometry that provides a minimum of 5% reduction in skin friction drag. To create the geometry, a program was written in Python that interfaced with Ansys Geometry Modeler. This program used the cylinder dimensions to inform the CAD backend of how to create a 3D representation of the domain with the row of protruding cylinders on the surface of the flat plate, the periodic sidewalls, and other domain features, scaled appropriately to account for the diameter, width, and spacing specific to each case. The computational domain extended 0.5 m in the axial direction, three boundary-layer thicknesses in the vertical direction, and varied based on the step-cylinder configuration in the spanwise direction. Each row created on the surface had three-cylinder segments, and sequential row numbers of 1, 3, and 20 rows were investigated. While the geometrical dimensions and spacing of the cylinders were changed to obtain optimized parameters, the spacing between the cylinders' rows for multi-row cases was fixed at one diameter, such that the tangent edges of sequential cylinder rows were aligned. The geometry generator was called on demand to generate each next test case as each prior case was completed. Case geometry was generated programmatically to allow for feedback in the optimization process, where geometry parameters could be modified in subsequent simulations based on the results of prior simulations. After the CAD representation of the domain was available, it was passed to a second Python program that directly communicated with the Ansys Fluent meshing server process. The second program controlled the grid generator by scaling mesh elements based on the feature sizes of the case geometry. Figure 4 shows a typical numerical grid for a single-row case and a close-up grid for a multiple-row case.

Figure 3. Parametric Optimization Process

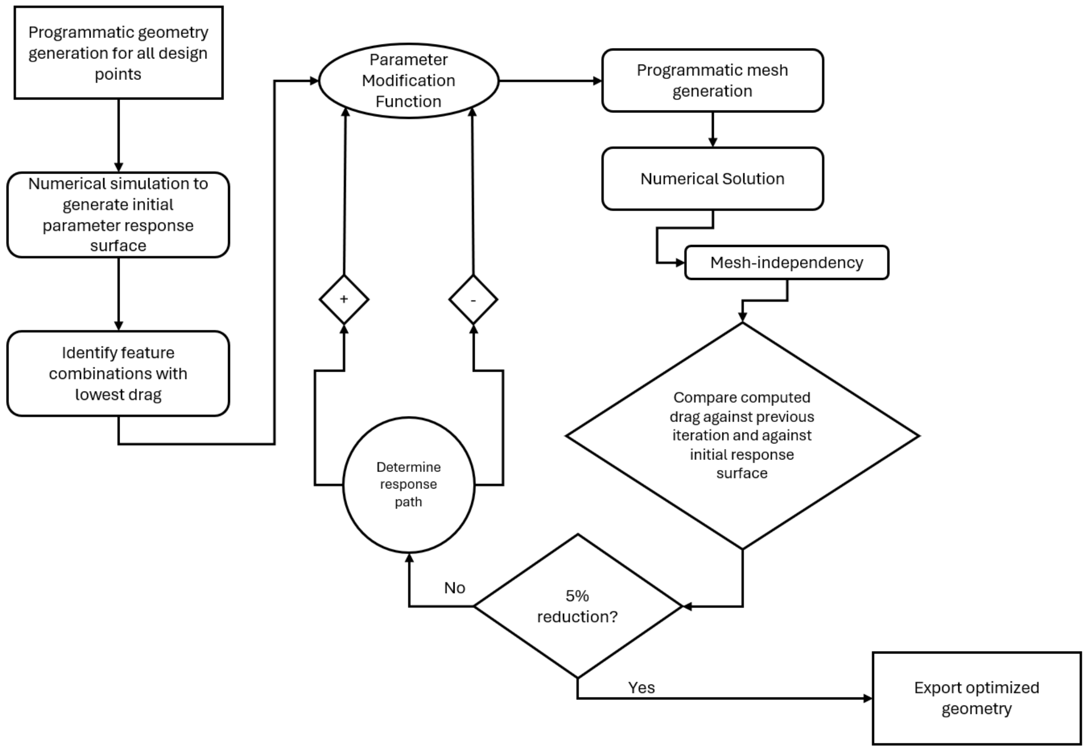

Figure 4. The Numerical Grid

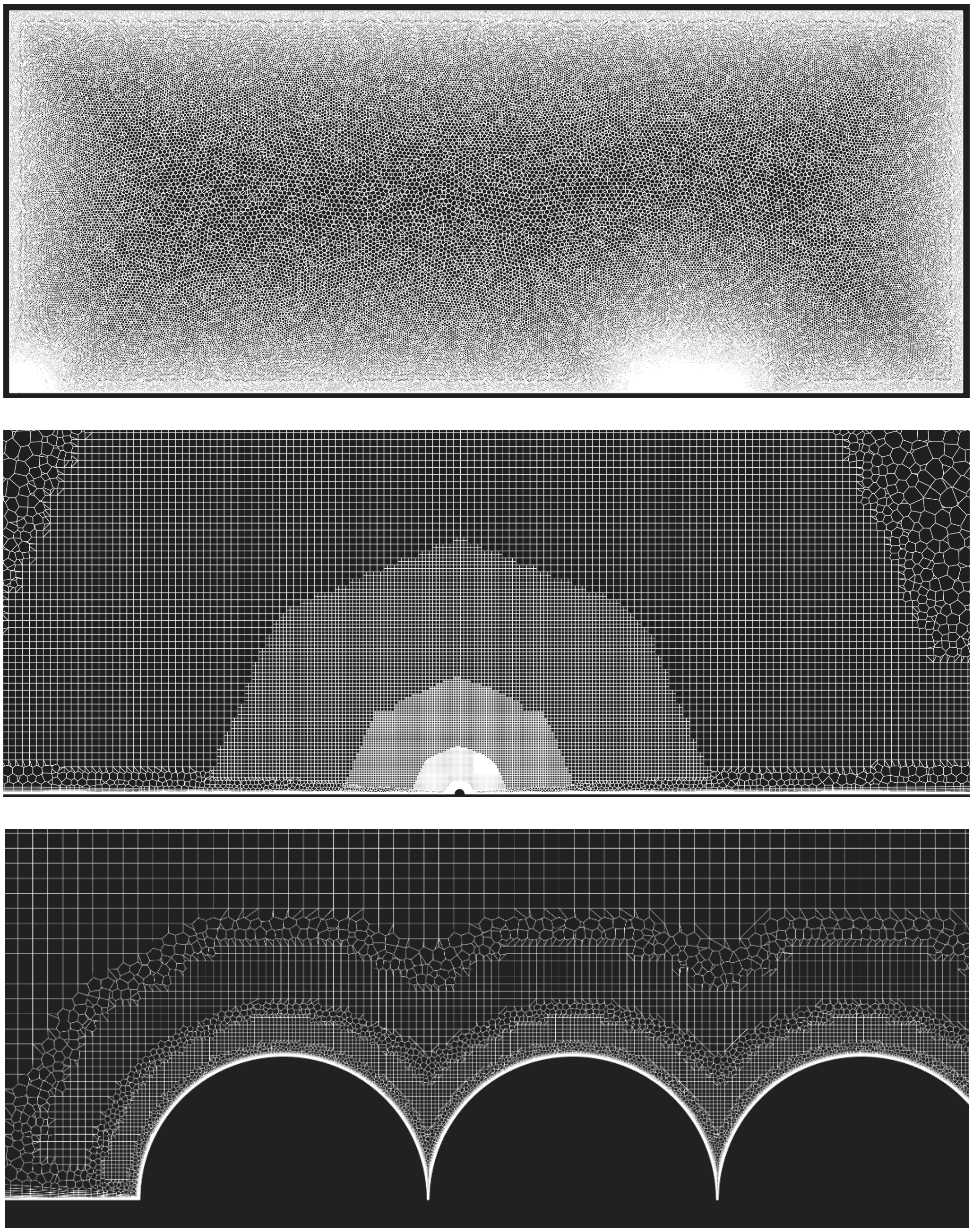

From the grid independence test using the skin friction coefficient as the monitoring parameter, the grid element size over the cylinders was 2% of the cylinder diameter. A total of 20 near-wall layers were used above the flat plate and the half-stepped cylinder surfaces. The cell counts ranged from 1 million to 20 million, depending on the geometrical dimensions of the cylinders. The generated grid was then passed to a third Python program that interfaced with Ansys Fluent Numerical Solver to apply the boundary conditions, create monitors for extracting data, and iterate to a converged solution.

Figure 5 shows the locations of the flow quantities and skin friction measurements. The monitors were generated at locations as a function of cylinder diameter. Vertical profile monitors were placed at 2D increments from -30D upstream to 50D downstream. Local skin friction surface monitors were placed on the flat plate from -10D upstream to the leading edge of the cylinders, in the spacing between the cylinders, and from the trailing edge of the cylinders to +10D downstream. A local skin friction surface monitor was also placed over the top surface of the cylinders spanning the entire half-circumference of the wetted area. In these surface monitors, the area-weighted skin friction was calculated using the following equation:

$$C_{f,area} = \frac{\sum(C_{f,i} \cdot A_i)}{\sum A_i}$$

Here, A_i is the local cell face area and $C_{f,i}$ is the corresponding skin friction coefficient computed using the velocity at the first cell near the wall. The separation of monitoring locations was done to provide more detailed information about the performance of each case with respect to riblet theory and microcavity behavior. Case subsets were chosen to encompass the boundaries of the diameter-spacing-width configuration space to inform the direction where an optimal geometry could be found via parameter modifications. A linear displacement function was chosen for speed, where each dimension was varied by a delta of 0.4 mm. The parameter modification function adjusted the cylinders' dimensions, created new geometry CAD representations, and repeated the mesh generation and numerical simulations with mesh independence assessment to find new skin friction drag coefficients. If the results were less than 5% reduction, the results were fed through the parametric modification function again for geometrical adjustments, and the process was repeated until a minimum of 5% reduction in the skin friction was achieved. The results were then finalized.

Reynolds-Averaged numerical simulations were performed using the commercial software Ansys-Fluent with the k-KL-omega turbulence model. This three-equation model separates laminar kinetic energy k_l and turbulent kinetic energy k_t to effectively capture laminar-turbulent transitional flow regimes and has been shown to match experimental transition in zero-pressure-gradient flat plate experiments. The inlet boundary condition was mapped from a plain flat plate turbulent boundary layer to ensure the incoming flow would be fully developed at the location of the half-stepped cylinders. This was confirmed by the data in Figure 6 and Table 1.

The outlet of the domain was set to a pressure-based outlet with zero-gauge static pressure to prevent any backflow or pressure fluctuations. The outlet was placed at least 250D or four boundary layer thicknesses from the trailing edge of the last row of cylinders to ensure reflections would not influence results. The spanwise sidewalls of the domain had a periodic boundary condition, which maps the calculated flow properties from each wall onto the other, thus creating a numerical domain that emulates an infinitely repeating span. The ceiling of the domain had a symmetric boundary condition applied to prevent reflections and remove any influence on the freestream velocity from the presence of a boundary. The total time spent generating grids was 32.9 hours, and the solution time of all cases presented here was 379.5 hours on a 512-core HPC server. All unscaled residuals reached convergence at or below 1e-5.

Figure 5. Locations of the Flow Quantity Profiles and Skin Friction Measurements

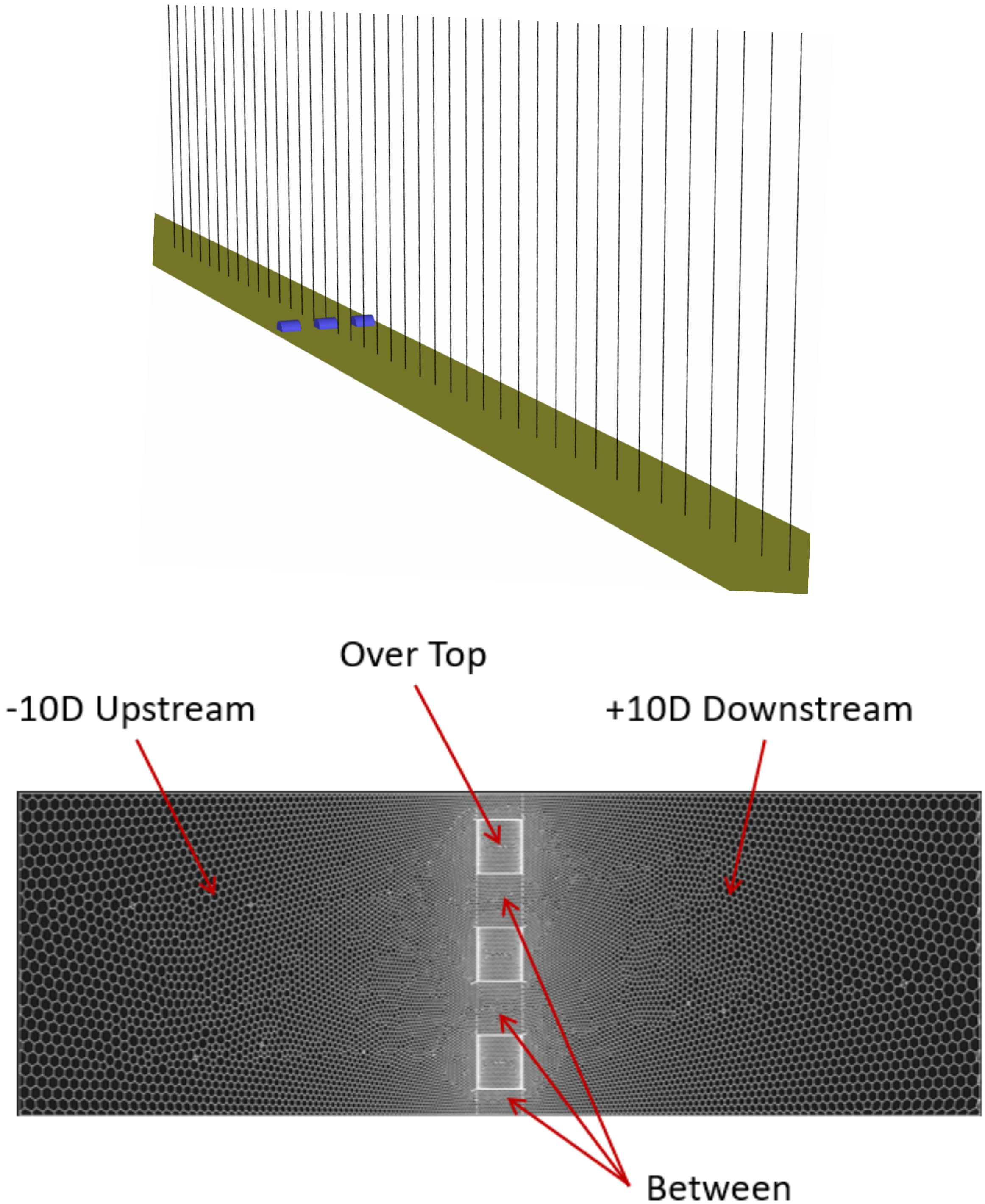

2.3. Turbulent Boundary Layer

Figure 6 shows selected normalized boundary layer profiles from all cases investigated at 2D upstream of the cylinders. The vertical distances were normalized by the boundary layer thickness (δ), and the mean velocity u was normalized by the freestream mean velocity, Uinf, which was 10 m/s for all cases. In total, more than 1000 cases have been investigated. The range for the cylinder's diameter was 0.0002 m to 0.0018 m, 0.0002 m to 0.0054 m for the spacing, and 0.0002 m to 0.001 m for the width. For all cases, the profiles display a typical turbulent boundary layer profile at zero pressure gradient. Table 1 shows the boundary layer parameters at this location. The skin friction was calculated from the surface shear stress and was used as a reference value for estimating the changes in the average skin friction for the half-stepped cylinders.

Figure 6. The Normalized Boundary Layer Profiles at 2D Upstream of the Half-Stepped Cylinders

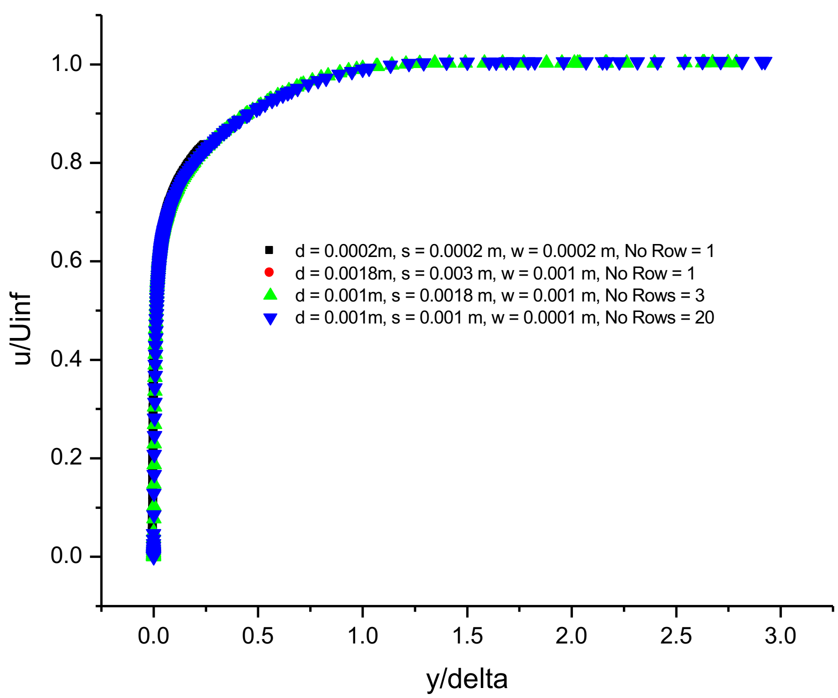

Table 1. Turbulent Boundary Layer Parameters

Boundary Layer Thickness (m), δ	0.079
Displacement Thickness (m), δ*	0.0090
Momentum Thickness (m), θ	0.007
Shape Factor, H = δ*/ θ	1.29
Skin Friction, Cf	0.0029

3. Results and Discussions

Figures 7 and 8 show the variation of the skin friction coefficient for the half-stepped cylinders with cylinder diameter and spacing, when the widths of the cylinders were 0.0002 m and 0.0006 m, respectively. Figure 9 shows the effects of changing diameter and the number of rows on the skin friction coefficient. Table 2 shows a summary of the skin friction coefficients and the percent changes when compared with the corresponding skin friction for the smooth flat plate turbulent boundary layer at zero pressure gradient. When the width is 0.0002 m, the lowest skin friction is associated with a diameter of 0.001 m and a spacing of 0.003 m. This case corresponds to 20 rows of cylinders with approximately 10% reduction in the skin friction. The rest of the cases are associated with one-row cylinders. For one-row cylinders, the lowest skin friction coefficients occur when the diameter, spacing, and width are 0.0002 m, with over a 7% reduction in the skin friction coefficient.

With spacing at 0.001 m, increasing the width to 0.0006 m increased the skin friction coefficient to higher than that of the smooth flat plate boundary layer, with the highest increase at 14% when the cylinder's diameter is at 0.0022 m. However, when the number of rows is increased to 20, and the spacing is 0.0046 m, there is more than a 7% drop in the skin friction coefficient.

Increasing the number of rows to three, with the cylinder's spacing and width at 0.001 m, resulted in a 15.8% to 16.6% decrease in the skin friction coefficient. When the number of rows increases to 20, the reduction in the skin friction coefficient is more than 33%.

Considering the radius of the cylinder as the height of the protrusions, when the diameter is less than 0.0018 m, the ratio of the radius to the boundary layer thickness is less than 1%. In a turbulent boundary layer, the dimensionless wall unit y^+ is defined as:

$$y^+ = y\,Rex\sqrt{\frac{C_f}{2}}$$

Previous investigations on riblets have shown that if the spacing between adjacent riblets is higher than 100 wall units, it prevents hairpin vortices from connecting to initiate unsteadiness and transition to a turbulent boundary layer, which has a higher skin friction. In our investigations, when the diameter and spacing are 0.001 m, the vertical protrusion is 81, and the spacing is 162 wall units, which is higher than 100 wall units identified in the riblet studies.

Figure 10 shows micro-cavities in superhydrophobic surfaces. To reduce the no-slip boundary condition, the width of the cavity should be greater than the viscous sub-layer thickness. Reducing the depth of the cavity or increasing the spacing between the cavity holes should also result in drag reduction. In our investigations, the spacing between subsequent rows that form the cavity holes is 0.002 m (2 mm), with a depth of 0.5 mm. The viscous sublayer thickness is estimated at 0.03 mm, which is much less than the width of the cavity. Given the depth and the width of the half-stepped cylinder surface, we hypothesized that both the spacing between the half-stepped cylinders and the cavity holes created by the rows of the cylinders contribute to the reduction of the skin friction coefficient. The increase in the number of rows to 20 has created significant cavities and boundary layer control for the highest reduction in the surface skin friction.

Figure 7. Skin Friction Variation with Diameter and Spacing (Cylinder Width = 0.0002 m)

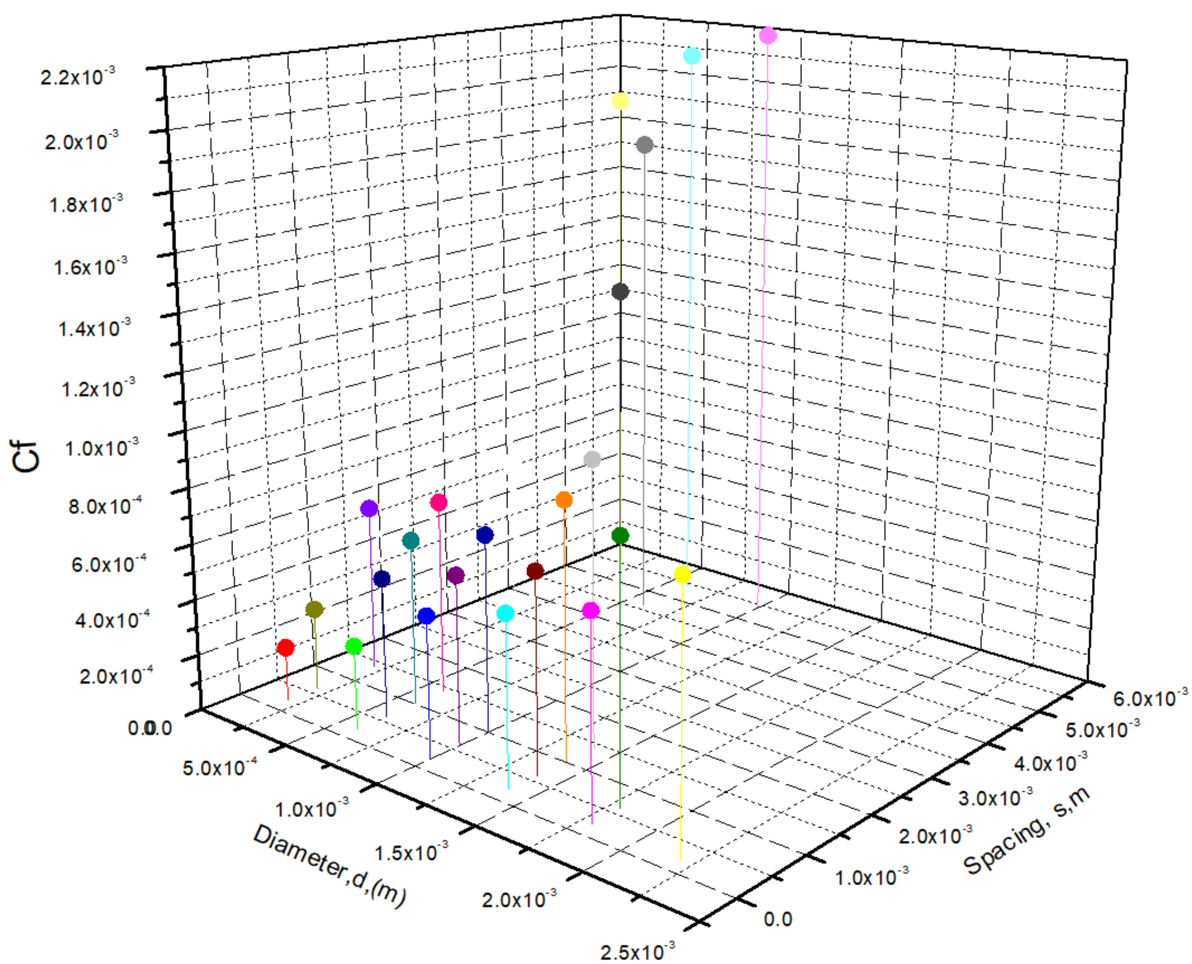

Figure 8. Skin Friction Variation with Diameter and Spacing (Cylinder Width = 0.0006 m).

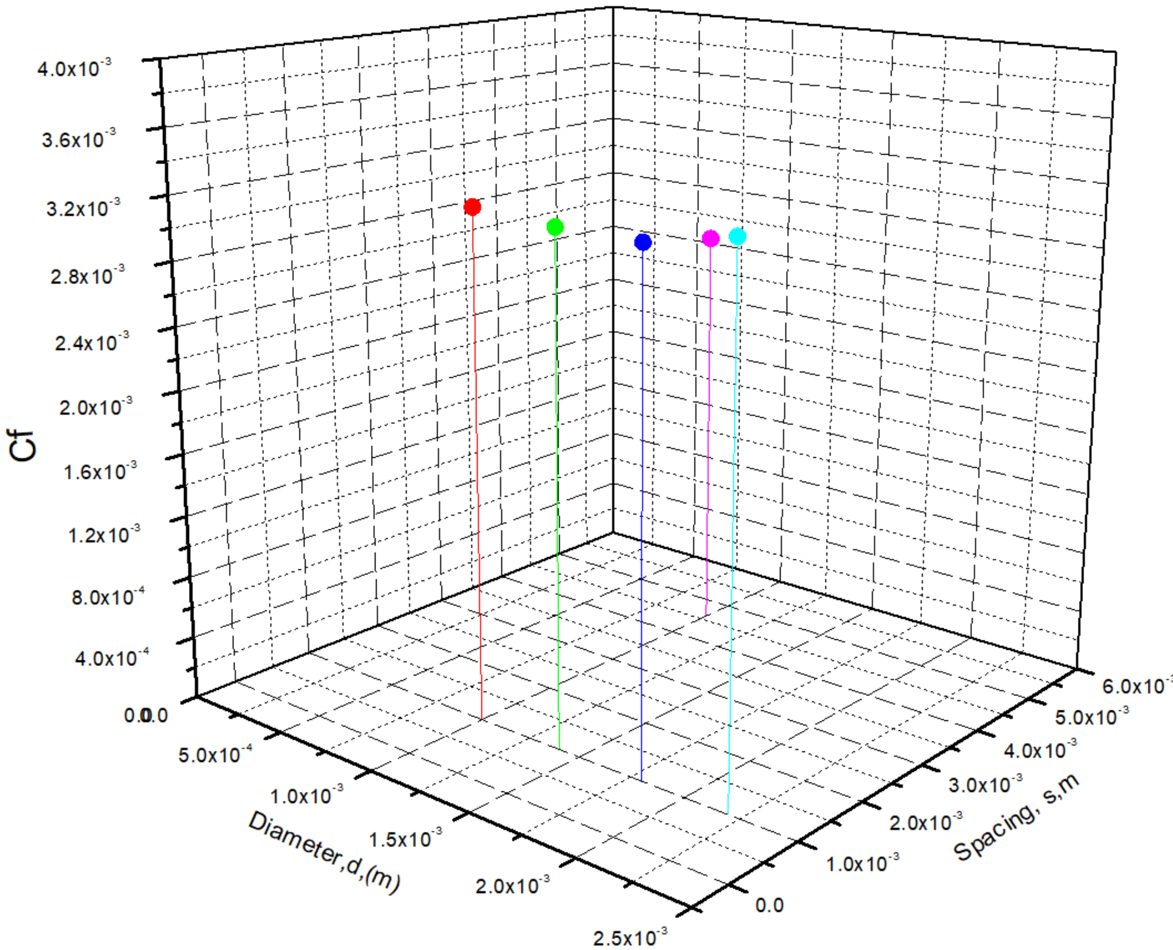

Figure 9. Skin Friction Variation with Diameter and Number of Rows (Cylinder Width and Spacing = 0.001 m).

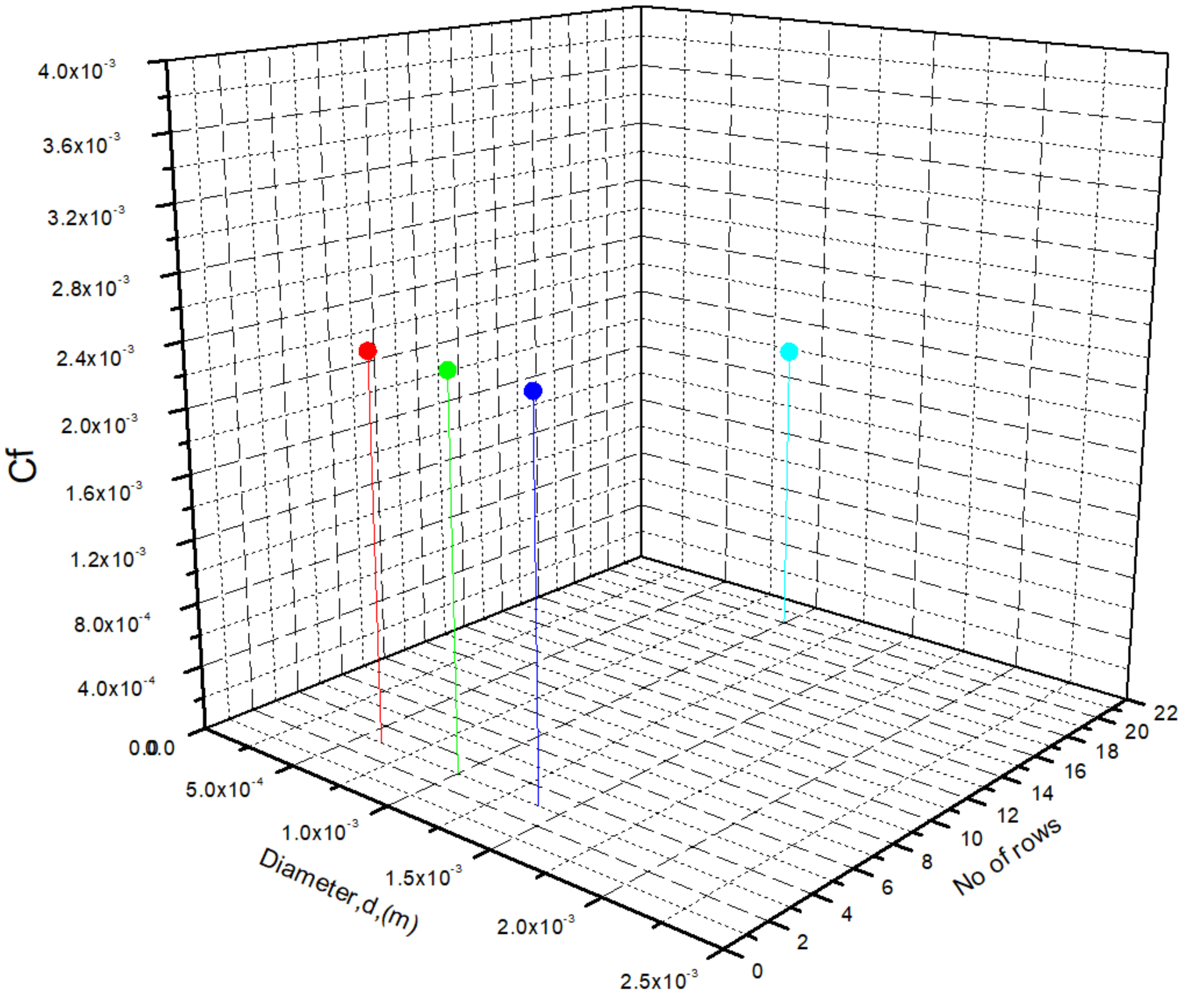

Table 2. The Change in Average Skin Friction with Diameter, Spacing, Width, and Number of Rows.

Diameter (m)	Spacing (m)	Width	N_rows		Skin Friction, Upstream	Skin Friction, Over	Skin Friction, Between	Skin Friction, Downstream	Average Skin Friction	% change
0.0002	0.0002	0.0002	1		0.0027	0.0027	0.0031	0.0023	0.0027	-7.6
0.0006	0.0002	0.0002	1		0.0025	0.0026	0.0041	0.0015	0.0027	-7.2
0.001	0.0002	0.0002	1		0.0024	0.0030	0.0045	0.0017	0.0029	0.2
0.0014	0.0002	0.0002	1		0.0023	0.0034	0.0046	0.0020	0.0031	7.9
0.0018	0.0002	0.0002	1		0.0022	0.0038	0.0046	0.0022	0.0032	11.8
0.0022	0.0002	0.0002	1		0.0021	0.0040	0.0046	0.0023	0.0033	13.4
0.0002	0.0006	0.0002	1		0.0027	0.0027	0.0030	0.0025	0.0027	-4.8
0.0006	0.0006	0.0002	1		0.0027	0.0027	0.0040	0.0022	0.0029	0.8
0.001	0.0006	0.0002	1		0.0027	0.0028	0.0046	0.0020	0.0030	4.5
0.0014	0.0006	0.0002	1		0.0026	0.0029	0.0049	0.0019	0.0031	7.1
0.0018	0.0006	0.0002	1		0.0026	0.0031	0.0050	0.0019	0.0031	9.2
0.0006	0.001	0.0002	1		0.0028	0.0028	0.0038	0.0025	0.0030	4.2
0.001	0.001	0.0002	1		0.0028	0.0029	0.0043	0.0024	0.0031	7.6
0.0014	0.001	0.0002	1		0.0028	0.0030	0.0046	0.0023	0.0032	9.7
0.0002	0.0014	0.0002	1		0.0028	0.0028	0.0030	0.0028	0.0029	-0.4
0.0006	0.0014	0.0002	1		0.0029	0.0029	0.0036	0.0026	0.0030	4.2
0.001	0.0014	0.0002	1		0.0028	0.0029	0.0040	0.0025	0.0031	6.8
0.0014	0.0014	0.0002	1		0.0028	0.0030	0.0042	0.0025	0.0031	8.7
0.0006	0.0046	0.0002	1		0.0029	0.0029	0.0031	0.0028	0.0029	2.3
0.0002	0.0054	0.0002	1		0.0029	0.0029	0.0029	0.0028	0.0029	-0.7
0.0006	0.0054	0.0002	1		0.0029	0.0029	0.0031	0.0029	0.0029	2.0
0.001	0.0054	0.0002	1		0.0029	0.0030	0.0032	0.0029	0.0030	5.1
0.001	0.003	0.0002	20		0.0028	0.0026	0.0023	0.0027	0.0026	-10.0
0.001	0.001	0.0006	1		0.0028	0.0028	0.0051	0.0021	0.0032	11.2
0.0014	0.001	0.0006	1		0.0027	0.0028	0.0052	0.0020	0.0032	10.1
0.0018	0.001	0.0006	1		0.0026	0.0028	0.0053	0.0020	0.0032	10.3
0.0022	0.001	0.0006	1		0.0026	0.0030	0.0054	0.0021	0.0033	14.4
0.001	0.0046	0.0006	20		0.0029	0.0026	0.0024	0.0027	0.0027	-7.4
0.001	0.001	0.001	1		0.0027	0.0030	0.0056	0.0020	0.0033	16.0
0.0014	0.001	0.001	1		0.0026	0.0029	0.0060	0.0022	0.0034	19.2
0.0018	0.001	0.001	1		0.0026	0.0030	0.0062	0.0022	0.0035	21.2
0.0018	0.003	0.001	1		0.0029	0.0030	0.0046	0.0026	0.0033	13.2
0.001	0.0046	0.001	1		0.0029	0.0029	0.0039	0.0027	0.0031	8.5
0.0006	0.001	0.001	3		0.0027	0.0026	0.0024	0.0020	0.0024	-15.8
0.001	0.001	0.001	3		0.0026	0.0026	0.0024	0.0019	0.0024	-16.6
0.0014	0.001	0.001	3		0.0026	0.0027	0.0023	0.0021	0.0024	-16.2
0.001	0.001	0.001	20		0.0024	0.0021	0.0012	0.0019	0.0019	-33.8

Figure 10. Micro Ridges in a Superhydrophobic Surface29.

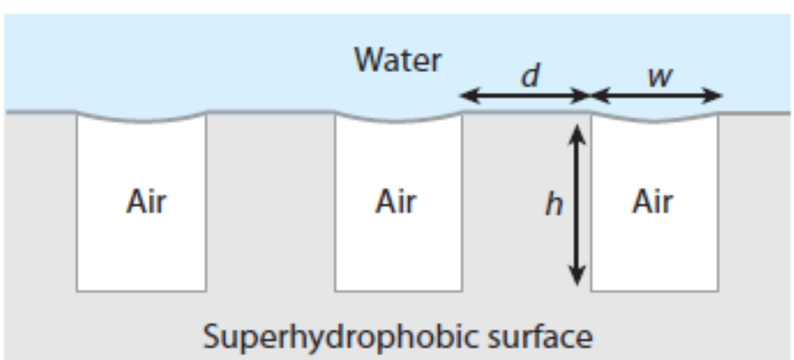

Figures 11-14 show the contour plots of the axial mean velocity, turbulent kinetic energy, and vorticity, along with the corresponding vector plots at different vertical distances above the half-stepped cylinder surface with 20 rows. The distances correspond to 0.13%, 0.26%, 0.52%, 0.78%, 1.04%, and 1.28% of the boundary layer thickness. At Y = 0.1 mm, the mean velocity is near zero within the cylinders, which corresponds to nearly zero TKE. Similar results are observed at Y = 0.2 mm, except that TKE increases in the wake of the cylinders downstream. The increase in TKE is in a wavy form and decreases downstream, which corresponds to increases in the mean velocity. These variations in TKE and mean velocity are amplified in the upper 0.50% of the boundary layer thickness, indicating that the half-stepped cylinders significantly displace the boundary layer in the vertical direction, thereby reducing the no-slip boundary condition and turbulence intensity near the surface.

Near the surface, at 0.13% of the boundary layer thickness, vorticity is high between the cylinder rows near the first two rows due to velocity acceleration and velocity gradients. However, it decreases to zero downstream and in the wake of the cylinders. With increasing vertical distance above 50% of the boundary layer thickness, these effects became less pronounced, and vorticity became more uniform between and above the cylinder surfaces.

The vector plots indicate recirculation upstream and downstream of the cylinders, which corresponds to high pressure in front and low pressure downstream, resulting in additional form drag. However, there is also recirculation between tandem cylinders, similar to cavity-type flow, which shifts the low-velocity region above the cylinders, reducing the velocity gradients, shear stress, and skin friction drag.

These results indicate that the lower velocity gradients between the cylinder rows and the cavity flow created by tandem rows of cylinders support the initial hypothesis that optimized half-step cylinder surfaces created ridges for controlling the hairpin vortices and cavities for reducing no-slip boundary conditions for a significant overall surface drag reduction.

Figure 11. Contours of Normalized Axial Mean Velocity from 10D Upstream to 15D Downstream of the Half-Stepped Cylinders, (a) X-Z Planes, (b) X-Y Plane at Mid-Section

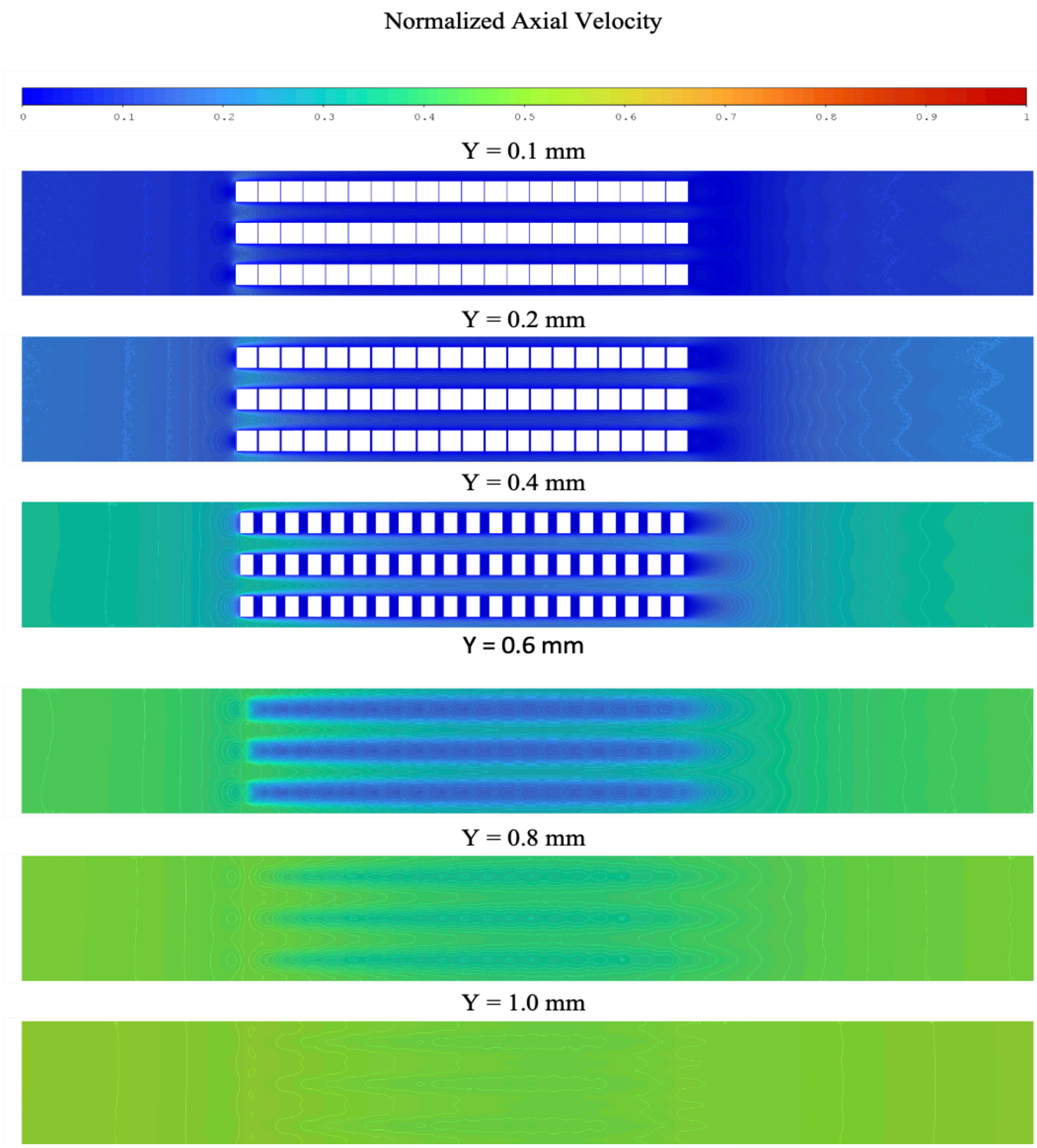

(a)

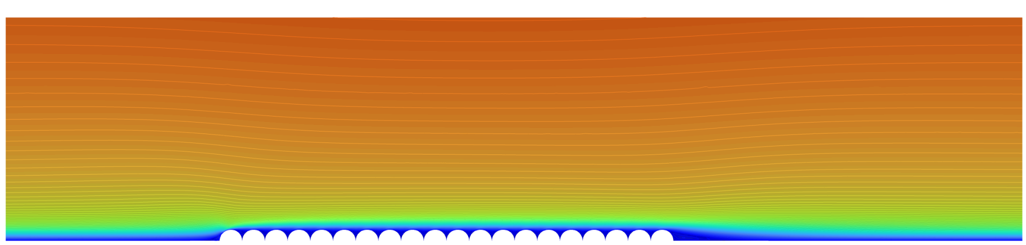

(b)

Figure 12. Contours of Normalized Turbulent Kinetic Energy Velocity from 10D Upstream to 15D Downstream of the Half-Stepped Cylinders, (a) X-Z Planes, (b) X-Y Plane at Mid-Section.

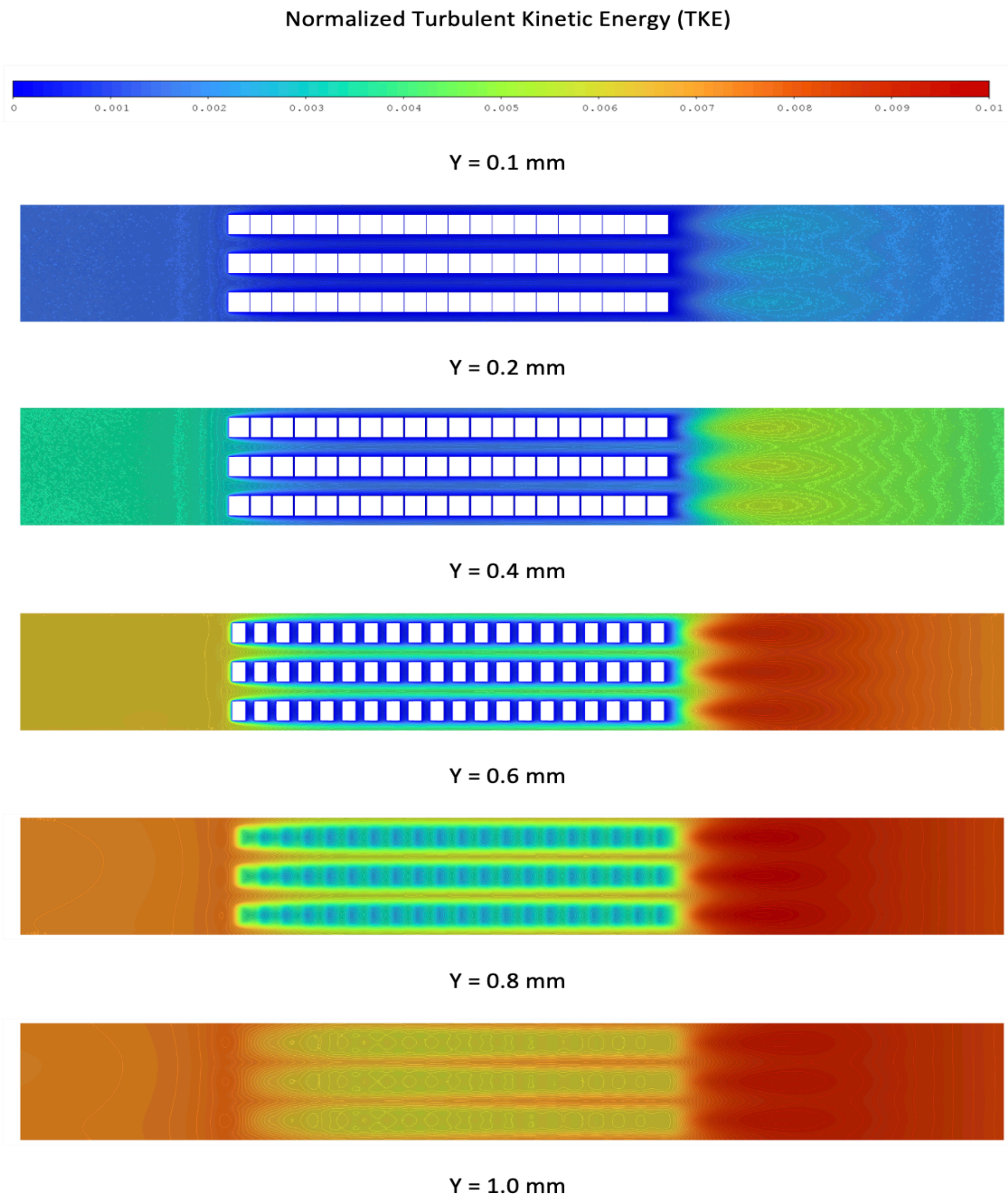

(a)

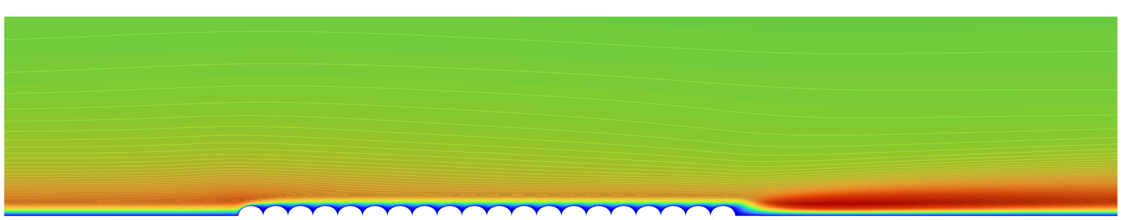

(b)

Figure 13. Contours of Vorticity

Vorticity Magnitude, s^-1

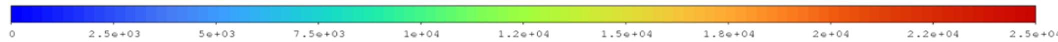

Y = 0.1 mm

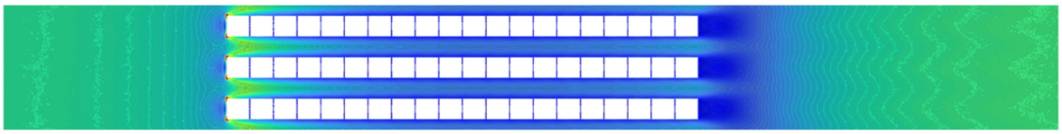

Y = 0.2 mm

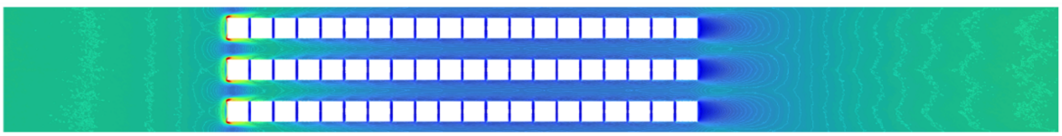

Y = 0.4 mm

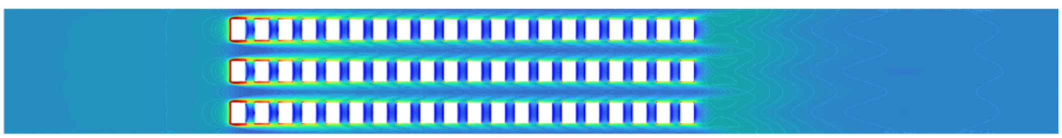

Y = 0.6 mm

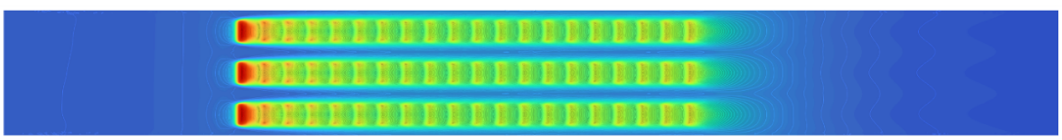

Y = 0.8 mm

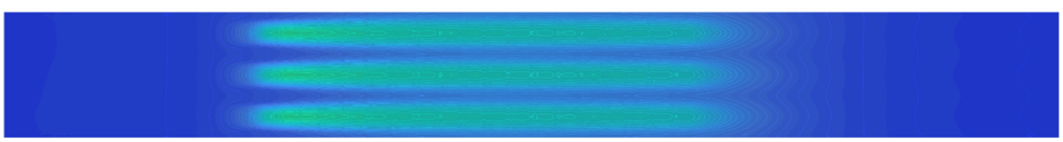

Y = 1.0 mm

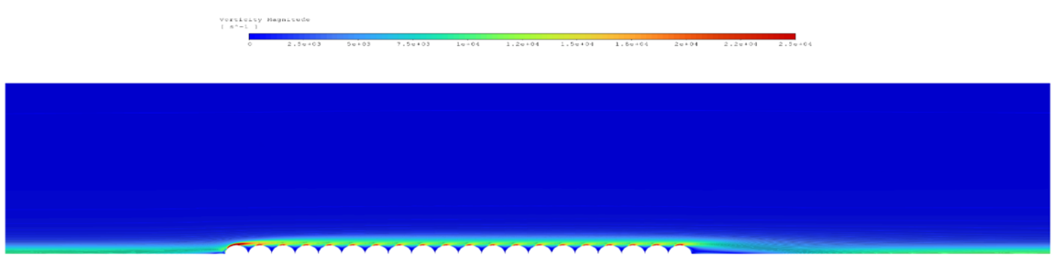

Figure 14. Velocity Vectors, (a) First Four Rows, (b) Last Three Rows

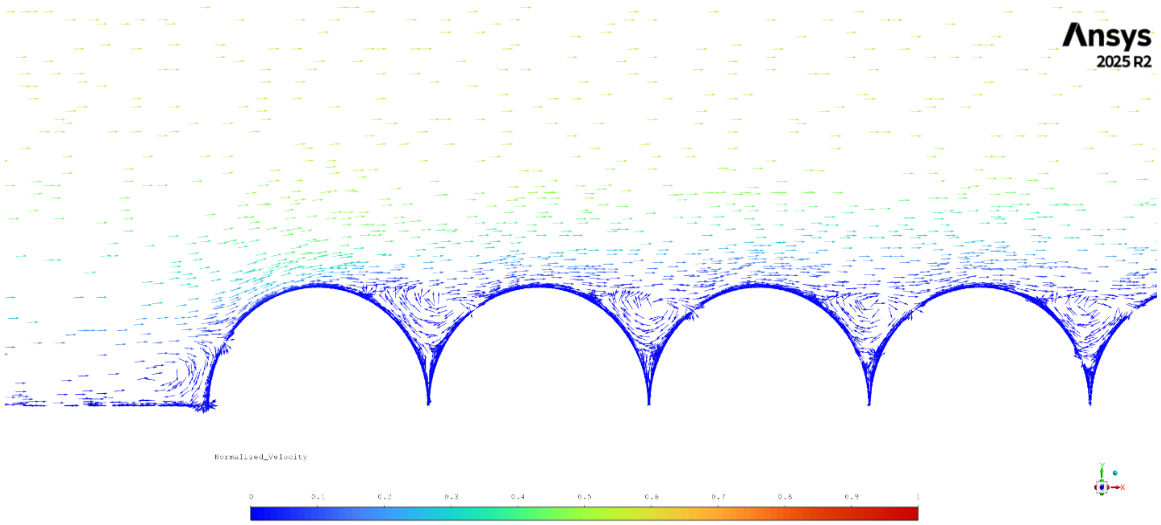

(a)

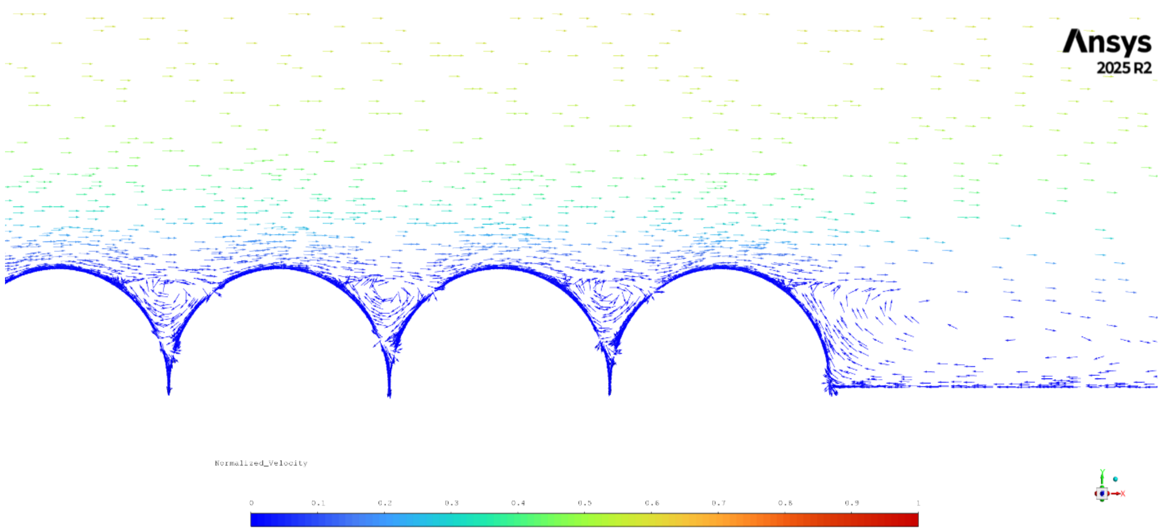

(b)

4. Summary & Conclusions

Parametric studies using computational fluid dynamics have been performed to identify optimized parameters of the half-stepped cylinders for reducing the skin friction of a turbulent boundary layer. The goal of the investigations was 1) to create ridges with half-stepped cylinder rows to control the boundary layer hairpin vortices to relaminarize the turbulent boundary layer and 2) to create micro cavities with tandem cylinders for reducing the no-slip boundary conditions for a significant reduction in the surface skin friction coefficient.

A smooth flat plate of 5.5 m length with variable width, depending on the spacing between the adjacent cylinders, was used in the investigations. The surface was tripped with a 1 mm diameter round wire placed 10 mm from the surface leading edge. The studies were performed at a free-stream mean velocity of 10 m/s. The Reynolds number at x = 5 m axial, which corresponds to 0.3 m upstream of the first half-stepped cylinder row, was 2.85×10^6.

A half-stepped cylinder row had three adjacent cylinders. The parameters changed were the cylinder’s diameter, the cylinder’s width, and the spacing between the adjacent cylinders. The range of these parameters was 0.0002 m to 0.0018 m for the diameter, 0.0002 m to 0.0054 m for the spacing, and 0.0002 m to 0.001 m for the width. The number of rows tested was 1, 3, and 20.

Reynolds-averaged Navier-Stokes simulations were conducted using the commercial CFD software Ansys-Fluent in conjunction with the k-KL-Omega turbulence model. A total of 20 near-wall layers were used above the flat plate and the half-stepped cylinder surfaces. The cell counts ranged from 1 million to 20 million, depending on the cylinders' geometric dimensions. The skin friction coefficient was calculated from the wall shear stress. The averaged skin friction coefficient was obtained using the local skin friction coefficient upstream, in between, above, and downstream of the row of cylinders.

For a single row of cylinders, the skin friction coefficient decreased by more than 7% when the cylinder’s diameter, width, and spacing were at 0.0002 m (0.2 mm). The highest decrease for the skin friction coefficient was more than 33% for the 20-row cylinders with these dimensions at 0.001 m (1 mm). For this case, the simulation results indicated significant reductions in turbulence intensity and mean velocity gradient near the surface, resulting in reduced no-slip boundary conditions and laminar flow in these areas.

Bibliography and Notes

1. State of California. 2019. Executive Order N-19-19. Sacramento, CA: Off. Gov.

2. State of California. 2020. Executive Order N-79-20. Sacramento, CA: Off. Gov.

3. Bushnell DM, Hefner JN, eds. 1990. Viscous Drag Reduction in Boundary Layers. Washington, DC: AIAA

4. Gad-el-Hak M. 2000. Flow Control: Passive, Active, and Reactive Flow Management. Cambridge, UK: Cambridge Univ. Press

5. Stull FD, Velkoff HR. 1972. Effect of transverse ribs on pressure recovery in a two-dimensional subsonic diffuser. AIAA Pap. 72-1141

6. Lang AW, Jones EM, Afroz F. 2017. Separation control over a grooved surface inspired by dolphin skin. Bioinspir. Biomim. 12:026005

7. Mariotti A, Buresti G, Gaggini G, Salvetti MV. 2017. Separation control and drag reduction for boat-tailed axisymmetric bodies through contoured transverse grooves. J. Fluid Mech. 832:514–49

8. Kairouz KA, Rahai HR. 2005. Turbulent junction with an upstream ribbed surface. Int. J. Heat Fluid Flow 29:771–79

9. Gada K, Rahai H. 2023. Numerical investigation of the NASA high-lift airfoil with a conformal vortex generator at transonic speed. SAE Tech. Pap. 2023-01-0979. doi:10.4271/2023-01-0979

10. García-Mayoral R, Jiménez J. 2011. Drag reduction by riblets. Philos. Trans. R. Soc. A 369:1412–27

11. Sareen A, Deters RW, Henry SP, Selig MS. 2014. Drag reduction using riblet film applied to airfoils for wind turbines. J. Sol. Energy Eng. 136:021007

12. Khader M, Sayma A. 2018. Drag reduction within radial turbine rotor passages using riblets. Proc. Inst. Mech. Eng. Part E [vol./pp. not given in source]

13. Raayai-Ardakani S, McKinley GH. 2019. Geometric optimization of riblet-textured surfaces for drag reduction in laminar boundary layer flows. Phys. Fluids 31:053601

14. Houshmand D, Youngs R, Wallace J, Balint J. 1983. An experimental study of changes in the structure of a turbulent boundary layer due to surface geometry changes. AIAA Pap. 83-0230

15. Rossiter J. 1964. Wind-tunnel experiments on the flow over rectangular cavities at subsonic and transonic speeds. Rep. Memo. 3438, Aeronaut. Res. Counc., Br. Minist. Aviat., London

16. Rockwell D, Naudascher E. 1979. Self-sustained oscillations of impinging free shear layers. Annu. Rev. Fluid Mech. 11:67–94

17. Morel T. 1979. Experimental study of a jet-driven Helmholtz oscillator. ASME J. Fluids Eng. 101:383

18. Gharib M, Roshko A. 1987. The effect of flow oscillations on cavity drag. J. Fluid Mech. 177:501–30

19. Murray N, Sällström E, Ukeiley L. 2009. Properties of subsonic open cavity flow fields. Phys. Fluids 21:095103

20. Boomsma A, Sotiropoulos F. 2016. Direct numerical simulations of sharkskin denticles in turbulent channel flow. Phys. Fluids 28:035106

21. Mao Q, Wang P, He C, Liu Y. 2021. Unsteady flow characteristics behind a shark denticle replica on the wall: time-resolved particle image velocimetry measurements. Phys. Fluids 33:075109

22. Sotoudeh F, Mousavi SM, Karimi N, Lee BJ, Abdolfazli-Esfahani J, Manshadi MKD. 2023. Natural and synthetic superhydrophobic surfaces: a review of the fundamentals, structures, and applications. Alex. Eng. J. 68:587–609

23. Rothstein JP. 2010. Slip on superhydrophobic surfaces. Annu. Rev. Fluid Mech. 42:89–109

24. Göhl J, Mark A, Sasic S, Edelvik F. 2018. An immersed boundary based dynamic contact angle framework for handling complex surfaces of mixed wettabilities. Int. J. Multiph. Flow 109:164–77

25. Daniello R, Waterhouse NE, Rothstein JP. 2009. Turbulent drag reduction using superhydrophobic surfaces. Phys. Fluids 21:085103

26. Voronov RS, Papavassiliou DV, Lee LL. 2008. Review of fluid slip over superhydrophobic surfaces and its dependence on the contact angle. Ind. Eng. Chem. Res. 47:2455–77

27. Lauga E, Brenner MP, Stone HA. 2007. Microfluidics: the no-slip boundary condition. In Handbook of Experimental Fluid Dynamics, ed. J Foss, C Tropea, AL Yarin, pp. 1219–40. New York: Springer

28. Ou J, Perot JB, Rothstein JP. 2004. Laminar drag reduction in microchannels using ultrahydrophobic surfaces. Phys. Fluids 16:4635–60

29. Ou J, Rothstein JP. 2005. Direct velocity measurements of the flow past drag-reducing ultrahydrophobic surfaces. Phys. Fluids 17:103606

30. Kumar M, Bhardwaj R. 2020. Wetting characteristics of *Colocasia esculenta* (taro) leaf and a bioinspired surface thereof. Sci. Rep. 10:935

31. Moffit R, Rahai HR. 2024. Investigations of a half-stepped cylinder in a turbulent boundary layer. Pap. FEDSM2024-130551, Proc. ASME 2024 Fluids Eng. Div. Summer Meet., Anaheim, CA, Jul. 15–17

About the Authors

Ryan Moffit

Mr. Ryan Moffit is a graduate student in the joint PhD program between California State University, Long Beach (CSULB) College of Engineering and the Claremont Graduate University (CGU) and a research assistant at the Center for Energy and Environmental Research & Services (CEERS) in the College of Engineering at CSULB. His research is focused on finding an optimized surface geometry for reducing the drag of vehicles. He has authored and co-authored two ASME conference papers and a recent presentation on reducing viscous drag of a boundary layer using a half-stepped cylinder surface at the SAE Aerotech 2026 conference in West Palm Beach, Florida.

Hamid Rahai, PhD

Dr. Hamid Rahai is a professor in the Department of Mechanical and Aerospace Engineering & Environmental Engineering and is the director of the Center for Energy and Environmental Research & Services (CEERS) in the College of Engineering at California State University, Long Beach (CSULB). He has taught various classes at the undergraduate and graduate levels in thermal sciences, supervised over 80 M.S. theses and projects and Ph.D. dissertations, and published more than 100 technical papers. He is the owner and co-owner of ten awarded and pending patents in wind energy, ambient and tailpipe NOx reductions, and aerodynamics drag reduction. He has been the principal and co-principal investigator of 72 grants and contracts from federal and state agencies and industry for over 15 million dollars. Dr. Rahai is the recipient of the 2004 Northrop Grumman Excellence in Teaching Award and the 2012 CSULB Impact Accomplishment of the Year in RSCA. He received the Outstanding Engineering Educator Award from the Orange County Engineering Council in California in 2014, and in 2019 he was inducted as a senior member of the National Academy of Inventors (NAI).

Komal Gada, PhD

Dr. Komal Gada is a senior researcher at the Center for Energy and Environmental Research & Services (CEERS) in the College of Engineering at CSULB. Dr. Gada specializes in numerical optimization and computational analyses. His research is focused on the effects of coil inserts on a pipe-jet in crossflow, vehicle drag reduction, and particle transport within confined spaces. He has authored ten journal and conference papers.

MTI MINETA TRANSPORTATION INSTITUTE